X-ray fibre diffraction analysis of assemblies formed by prion-related peptides: Polymorphism of the heterodimer interface between PrP^{C} and PrP^{Sc}

Hideyo Inouye and Daniel A. Kirschner*

Biology Department, Boston College, Chestnut Hill, MA 02467-3811

**Author for correspondence*

Fibre Diffraction Review **11**, 102-112, 2003

ABSTRACT

The molecular mechanism in prion diseases involves structural alteration of the non-infectious cellular isoform (PrP^{C}) to the infectious, scrapie isoform (PrP^{Sc}). The structural transition is thought to involve a binding interface between the two isoforms in their N-terminal domains. Because prions and prion-related peptides can form amyloid-like fibrillar assemblies, we have used X-ray fibre diffraction to study the structure of the binding interface in synthetic peptides that have sequence similarity with the prion protein (PrP). Our previous studies show that the alanine-rich peptides PrP106-122 and PrP109-122 form slab-like structures that are stacked as one-dimensional lattices having cumulative disorder. The unit cell is a four-stranded β-sheet with the chains directed along the stacking direction. Neighboring β-sheets are quarter-staggered (like in β silk). Electron density projections indicate that the peptides form a reverse turn with the larger residues in the N-terminal domain distinguishable from the alanine-rich C-terminal domain. This reverse turn accounts for the 33 Å-length of β chains (or slab thickness) as measured from the low-angle scattering. In this report, we considered three different inter-molecular packings for the reverse turn molecules: i.e., anti-parallel, parallel, and staggered. The staggered arrangement gave the best agreement between the observed and calculated X-ray intensities. From the molecular model we suggest that the autocatalytic replication of prions may involve hydrogen-bonding between intermolecular antiparallel β chains of the alanine-rich domains at the binding interface between PrP^{C} and PrP^{Sc}.

Key words: Prion; amyloid; X-ray diffraction; reverse turn; beta-pleated sheet

Introduction

X-ray diffraction has been used to study the molecular organization of amyloid-like structures formed by the N-terminal domains of the prion protein (Figures 1 and 2) - including those of Syrian hamster (SHa; PrP27-30 or SHa90-231; SHa90-145; SHa106-122; "H1" or SHa109-122; "A8A" or SHa113-120); mouse (Mo; Mo89-143); and human Gerstmann-Sträussler-Scheinker or GSS type mutations expressed in mouse or Syrian hamster sequences (Mo89-143(P101L); SHa104-122(3A-V)) (Nguyen *et al.*, 1995; Inouye and Kirschner, 1997, 1998; Inouye *et al.*, 2000). As reported in these studies, X-ray fibre and powder diffraction (Figure 3) shows that the N-terminal domain in PrP is folded as a β-sheet which is the likely conformation for the PrP^{Sc} isoform (Pan *et al.*, 1993). On the other hand, solution NMR indicates an α helical-rich structure and an N-terminal domain (90-~125) that is "flexibly disordered" (Figure 2) (Riek *et al.*, 1996; James *et al.*, 1997; Donne *et al.*, 1997; Liu *et al.*, 1999; Lopez *et al.*, 2000; Zahn *et al.*, 2000). X-ray single crystal analysis gives a similar monomeric structure as shown by solution NMR, but does not resolve a structure for the N-terminal residues 90-119 (Knaus

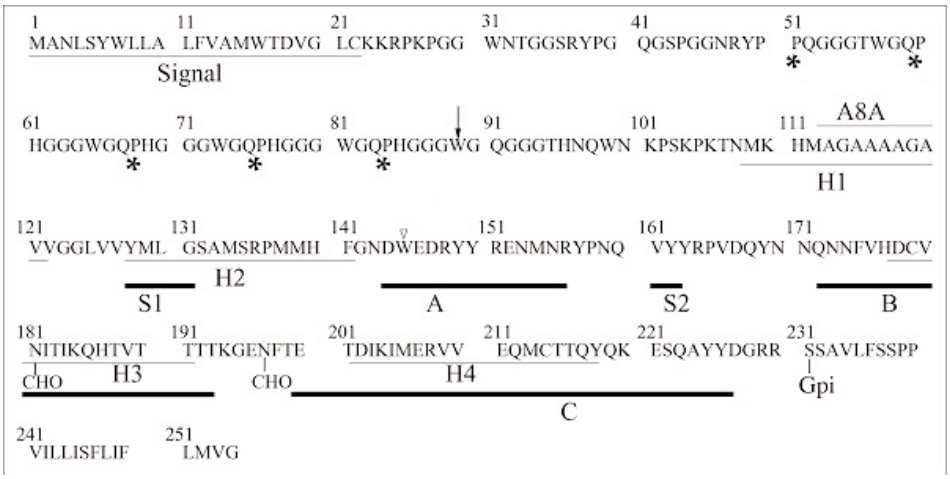

Figure 1. Primary structure of hamster prion protein (Stahl *et al*., 1993; Inouye and Kirschner, 1998). The first N-terminal 22 residues are the signal sequence. While PrP^{C} is completely digested by proteinase K, PrP^{Sc} is partially digested yielding PrP27-30 (Prusiner *et al*., 1983) which starts with residue 90 (black arrow). The glycosylation sites at residues 181 and 197 are indicated by -CHO, and the glycosylphosphatidylinositol anchor is shown at residue 231 by Gpi. A stop codon has been found for the human prion gene at 145 (open arrowhead) (Kitamoto *et al*., 1993). The N-terminal octarepeats (*) are likely Cu binding sites (Viles *et al*., 1999). The four predicted helices (H1,H2,H3 and H4) are shown, as are the helical domains A, B and C, and b chains S1 and S2 as determined by solution NMR (James *et al*., 1997). X-ray fibre diffraction studies on domains H1, A8A and SHa106-122 are discussed in this paper.

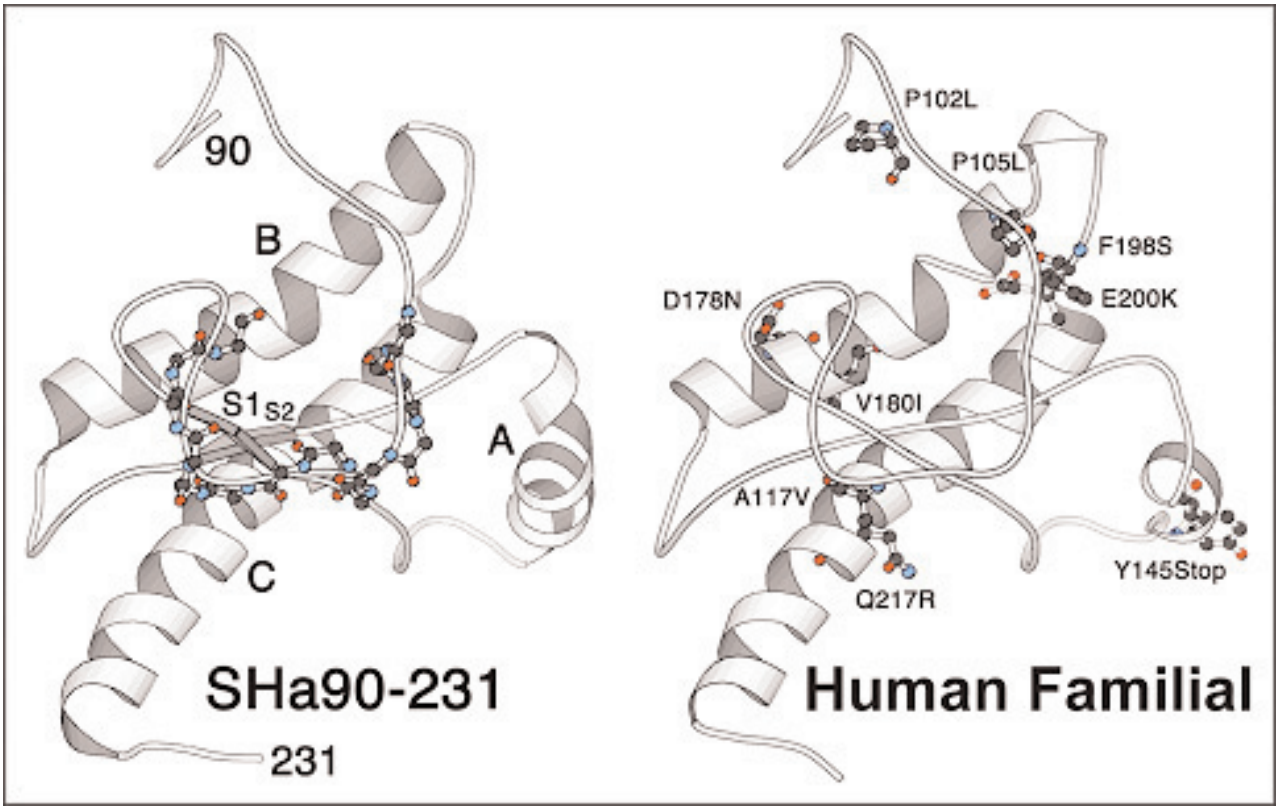

Figure 2. Molscript representation of PrP. (**Left**) Location of the peptide fragments in Syrian hamster 90-231 (SHa90-231). H1 domain (SHa109-122; shown as ball and stick model) as determined by solution NMR (James *et al*.,1997). The N-terminal domain is flexibly disordered, while the C-terminal domain contains three a helical domains (A, B, C), and two short β strands (S1, S2). The 3F4 epitope domain is at the N-terminal end of the ball and stick model, and alanine-rich A8A is at the C-terminal end. If A8A forms a β strand, then A8A, S1, and S2 are likely to be H-bonded together, forming a β sheet. (**Right**) The three-dimensional structure of human PrP as predicted by Swiss Modeler (Guex *et al*., 1999) using the NMR hamster PrP structure (left panel) as a template. The mutations in human familial prion disease including Gerstmann-Sträussler-Scheinker syndrome (GSS), familial Creutzfeldt-Jakob disease (CJD), and fatal familial insomnia (FFI) are indicated (Prusiner, 1991). Formation of a β sheet is likely facilitated by these mutations. X-ray fibre diffraction of peptides containing the GSS type P102L and A117V substitutions appears to confirm this (Inouye *et al*., 2000).

et al., 2001). The α helical structure may be present in the PrP^C isoform.

Peptide fragment SHa109-122 (designated H1), which is at the binding interface between PrP^C and PrP^{Sc}, shows two different diffraction patterns depending on the treatment or physical state of the sample, i.e., lyophilized or solubilized in 50% acetonitrile (AcN) solution followed by drying (Nguyen *et al.*, 1995). With the latter treatment, the N-terminal part of H1 - i.e., the epitope region (residues 109-112: MKHM) for the 3F4 antibody-is likely to be folded as a β chain while in the former state the epitope is not in the β conformation and is probably exposed on the protein surface (Nguyen *et al.*, 1995; Inouye and Kirschner, 1998; Inouye *et al.*, 2000). The two conformations indicated by the X-ray diffraction and NMR data are consistent with the notion that PrP^{Sc} goes through a partial denaturation or unfolding when it interacts with PrP^C. The folding-unfolding transformation is evident in cell-free PrP replication, where treatment of PrP^{Sc} by guanidinium hydrochloride (GdnHCl) is required (Kocisko *et al.*, 1994) to expose the 3F4 epitope that is concealed in PrP^{Sc} (Safar *et al.*, 1998).

In this report we address the question of the folding of the H1 domain, which by harboring the 3F4 epitope is thought to be at or near the binding interface between the two PrP isoforms and therefore to play a crucial role in the $PrP^C \rightarrow PrP^{Sc}$ transition. We previously proposed three different molecular packings for H1 assemblies, i.e., anti-parallel, parallel, and staggered (Inouye *et al.*, 2000); however, atomic models were not tested against the observed X-ray intensity. Here, we first summarize our previous X-ray analysis and then extend it by fitting atomic models to the electron density map. Staggered inter-molecular packing of H1 monomers most closely fits the X-ray data, and suggests a role for hydrogen-bonding at the binding interface between PrP^C and PrP^{Sc}.

Materials and Methods

The experimental methods have been described in detail in our previous reports (Nguyen *et al.*, 1995; Inouye and Kirschner, 1997; Inouye *et al.*, 2000) and are given in brief here.

X-ray diffraction

Peptides and Samples. The sample peptides (sequences indicated Figure 1) were analyzed in the lyophilized state and after solubilization and drying, as previously described.

Data Collection and Analysis. X-ray diffraction patterns were recorded on film and digitized as described. The intensities were obtained from narrow strip scans along the equatorial, meridional or radial directions using the public domain NIH Image program on a Macintosh computer (developed at the U.S. National Institutes of Health and available on the Internet at http://rsb.info.nih.gov/nih-image/). The diffraction pattern showing slight orientation was treated as a powder pattern. The structure amplitudes are related to the observed intensity by Lorentz and polarization factors. The Lorentz factor L in powder diffraction, for example, is given by $\frac{\lambda}{4\sin\theta}$, where λ is X-ray wavelength and θ is half of the scattering angle (Cella *et al.*, 1970). As the spherically distributed intensity I_s is measured along the radial direction on flat film, the structure factor F is related to I_s by

$$I_s = \frac{F^2 LP}{2\pi R} = \frac{F^2 P}{4\pi R^2},$$

where

$$R = \frac{2\sin\theta}{\lambda}$$

and the polarization factor (Inouye *et al.*, 1993)

$$P = \frac{1+\cos^2 2\theta}{2}.$$

The lattice constants and indices were searched by comparing the observed and calculated spacings using different combinations of indices within a particular range of lattice constants and indices. The final values of lattice constants were determined by the least squares procedure.

Fourier synthesis iteration and molecular modelling

The Fourier procedure for fibre or powder diffractions has been described in detail (Inouye *et al.*, 1993; Inouye and Kirschner, 1996, 1997). In brief:

1. We first choose the initial phase model which defines the atomic fraction coordinates (x_j,y_j,z_j) for the *j*th atom in the unit cell, using initial phases derived from the Cα, Cβ, and peptide bonds of the β

silk backbone (Marsh *et al*., 1955).

2. Next, we calculate the structure factors $F_{calc}(hkl)$ within a given range of *h,k,l* and for the observed unit cell according to

$$F_{calc}(hkl) = \sum_j f_j \exp i2\pi(hx_j + ky_j + lz_j) \quad ,$$

where f_j is the atomic factor. We use space group P1 (which assumes no symmetry) and calculate the structure factors for both positive and negative indices. In this report, the orthogonal unit assigned to the peptides is not required by symmetry, but simply happens to be convenient.

3. We next combine the observed structure amplitudes $|F_{obs}(hkl)|$ and calculated phases $\phi_{calc}(hkl)$. For powder diffraction the observed intensity is given as the spherically distributed intensity $I_s(R)$ as a function of radial component of spherical reciprocal coordinates *R*. Since multiple indices may contribute to each peak in powder diffraction, the observed structure amplitudes for the specified indices are calculated by dividing the observed intensity in proportion to the calculated intensities from the model. The observed structure amplitudes are, therefore given by

$$\left|F_{obs}(hkl)\right|^2 = \frac{C(hkl)I_s(R)}{LP} \quad ,$$

where

$$C(hkl) = \frac{\left|F_{calc}(hkl)\right|^2}{\sum\left|F_{calc}(hkl)\right|^2}$$ and LP is the Lorentz-polarization factor (see above). The indices *hkl* for summation satisfies the condition $\left|R_{hkl}^{-1} - R^{-1}\right| < \Delta d$, where R_{hkl} is the radial component of the Bragg spacing in spherical coordinates, and Δd is a defined critical value between the observed and calculated Bragg spacings (usually 0.005 - 0.01 Å). The relative deviation between the observed and calculated structure amplitudes is given as

$$R_{obs-amp} = \frac{\sum\left|\left|F_{obs}\right| - \left|F_{calc}\right|\right|}{\sum\left|F_{obs}\right|} \quad .$$

4. Finally, we use the observed amplitudes and calculated phases to calculate the electron density map with XtalView (McRee, 1992), and we fit the density map with a molecular model built using Swiss-Modeler (Guex *et al*., 1999). In most cases, before building the molecular model, we optimized the phase from the β silk backbone in the Fourier iteration procedure by modifying the electron density distribution, i.e., setting the negative electron densities (on a relative scale) to zero (Nguyen *et al*., 1995; Inouye and Kirschner, 1997). The atomic model is then modified to fit the newly-derived electron density map. With the new atomic model, we then go back to Step (2), and iterate the process until the *R*-factor does not decrease further.

Molecular modelling

The three dimensional molecular model is displayed and manipulated with Molscript (Kraulis, 1991), XtalView (McRee, 1992), Rasmol (by Roger Sayle), Swiss-PDB Viewer (Guex, *et al*., 1999), and QUANTA (Accelrys, Inc., San Diego, CA, USA). The secondary structure is determined from the atomic coordinates using DSSP (Kabsch and Sander, 1983) and STRIDE (Frishman and Argos, 1995; http://www.embl-heidelberg.de/stride/stride_info.html).

Theory of one-dimensional disordered lattice

Some prion peptides assemble *in vitro* to form a slab-like structure. Stacking along the β chain direction of the slabs gives a strong reflection in the low-angle region, and subsequent broad intensity maxima. The former likely arises from the interference of the disordered lattice, and the latter arises from the Fourier transform of the unit structure. Since a single interference peak is observed - i.e., the interference curve rapidly approaches unity - the lattice is disordered. In the current report, correct measurement of the thickness of the slab gave a crucial constraint to the length of the extended β chain, indicating a reverse turn or hairpin. In the following we describe the Fourier transform of a one-dimensional lattice having cumulative or non-cumulative disorder. The formulation follows the case for a discrete helical array (Inouye, 1994). Here, the disorder parameter is included in the structure factor, whereas usually it is defined in the autocorrelation function. The advantage of this formulation is that the intensity function for a discrete helical array can be written in closed form (Inouye, 1994).

We first define a lattice-generating function with disorder, an auto-correlation function, and an intensity function for a one-dimensional lattice. The lattice position is defined by

$$r_j = jd + \delta_j \qquad (1)$$

where *d* is a distance between lattice points and δ_j is

a displacement from the ideal position. The lattice $\rho(r)$ is described as

$$\rho(r) = \sum_{j=0}^{N-1} \delta(r - r_j) , \qquad (2)$$

where N is the number of lattice points. The autocorrelation function, using (1) is

$$\rho(r) * \rho(-r) = \sum_{j=0}^{N-1} \sum_{k=0}^{N-1} \delta\left[r - (j-k)d - (\delta_j' - \delta_k')\right] . \quad (3)$$

Fourier transform of (3) gives the intensity function as

$$I(R) = N + \sum_{\substack{j=0 \\ j \neq k}}^{N-1} \sum_{k=0}^{N-1} \exp[i2\pi(j-k)dR] \exp\left[i2\pi(\delta_j' - \delta_k')R\right] , \quad (4)$$

where the summation in the second term is performed with $j \neq k$. Since the observed intensity refers to the intensity for a statistical average (denoted by < >) of the positional displacements, then

$$< I(R) >= N + \sum_{\substack{j=0 \\ i \neq k}}^{N-1} \sum_{k=0}^{N-1} \exp[i2\pi(j-k)dR] < \exp[i2\pi(\delta_j' - \delta_k')R] > \qquad (5)$$

To evaluate the averaged exponential term, we assume a probability distribution function for the positional displacements as shown below.

Perfect lattice. When there is no disorder, the intensity function is written as

$$I_0(R) = \sin^2(\pi N d R) / \sin^2(\pi d R) \qquad (6)$$

The intensity maxima N^2 occur periodically at $R=l/d$ where l is an integer and N/d is the integral peak area. The integral width of the reflection is thus $1/(Nd)$. When N is large, the intensity $I_o(R)$ is written using a delta function

$$I_0(R) = (N/d) \sum_{l=-\infty}^{\infty} \delta(R - l/d) \qquad (7)$$

according to the following relationship

$$\sum_{n=-\infty}^{\infty} \delta(x - n x_0) = (1/x_0) \sum_{m=-\infty}^{\infty} \exp(i2\pi m x / x_0) \qquad (8)$$

Non-cumulative disorder. Assuming that δ_j and δ_k are independent and the distribution of δ_j is Gaussian with zero mean and mean square displacement $<\delta^2>$ (Barakat, 1987), the statistical average of the displacement in (5) is given by

$$< \exp[i2\pi(\delta_j' - \delta_k')R] >=< \exp(i2\pi\delta_j' R) > \quad \text{and}$$

$$< \exp(-i2\pi\delta_k' R) >= \exp(-2M) , \qquad (9)$$

where $M = 2\pi^2 R^2 <\delta^2>$. The term (9) has been called a Debye-Waller factor for thermal disorder. From (5) the intensity is given as

$$< I(R) >= N + \exp(-2M) \sum_{\substack{j=0 \\ j \neq k}}^{N-1} \sum_{k=0}^{N-1} \exp[i2\pi(j-k)dR] . \quad (10)$$

Substituting j-k by m, and replacing the double sum by a single sum yields

$$< I(R) >= N + \exp(-2M) \sum_{m=1}^{N-1} (N-m)[\exp(i2\pi m d R) + \exp(-i2\pi m d R)] \qquad (11)$$

The intensity corresponds to an independent oscillator model of thermal disorder and to static disorder of the first kind. Including the intensity function of $I_o(R)$ for a perfect lattice, we rewrite (11) as

$$< I(R) >= I_0(R) \exp(-2M) + N[1 - \exp(-2M)] . \qquad (12)$$

The first term indicates that the Bragg intensity of the perfect lattice is reduced, and the second term contributes to the diffuse scattering.

Cumulative disorder. When the displacements δ_j' and δ_k' are not independent, Egelman and DeRosier (1982) and Barakat (1987) assumed that the deviation at the jth position is cumulative, then the jth displacement is written in terms of the previous ones as

$$\delta_j' = \sum_{t=1}^{j} \delta_t . \qquad (13)$$

Substituting this in (5) yields

$$< \exp[i2\pi(\delta_j' - \delta_k')R] >=< \exp[i2\pi R(\sum_{t=1}^{j} \delta_t - \sum_{t=1}^{k} \delta_t)] > , \quad (14)$$

which becomes $< \exp(i2\pi R \sum_{t=j+1}^{k} \delta_t) >$ for $k > j$, and $< \exp(i2\pi R \sum_{t=k+1}^{j} \delta_t) >$ for $k < j$. According to the multivariate characteristic function for zero-mean uncorrelated Gaussian random variables,

$$< \exp(\pm ib \sum_{t=m_1}^{m_2} a_t \delta_t) >= \exp[-b^2 < \delta^2 > (\sum_{t=m_1}^{m_2} a_t^2)/2] \qquad (15)$$

where a_t and b are constants, δ_t is a random variable, and $<\delta^2>$ is the mean square displacement (Barakat, 1987). Averaging over the δ_t in (14) leads to

$$< \exp[i2\pi(\delta_j - \delta_k)R] >= \exp(-2\pi^2 R^2 |j-k| < \delta^2 >) \quad \text{for } j \neq k \qquad (16)$$

This statistical average is the same as the one for a paracrystalline disorder of the second kind (Hosemann and Bagchi, 1962; Vainshtein, 1966; Inouye *et al*., 1989). Using this representation of the statistical average in (5), the intensity is given by

$$< I(R) >= N + \sum_{\substack{j=0 \\ j\neq k}}^{N-1}\sum_{k=0}^{N-1} \exp[i2\pi(j-k)dR]\exp(-2\pi^2 R^2 |j-k| < \delta^2 >) \quad (17)$$

Replacing the double sum by a single sum with $j\text{-}k=m\ (1 \le m \le N\text{-}1)$ yields

$$< I(R) >= N + \sum_{m=1}^{N-1}(N-m)[\exp(i2\pi mdR) + \exp(-i2\pi mdR)]\exp(-2\pi^2 R^2 m < \delta^2 >) \quad (18)$$

This gives a closed form for a finite number of N (Vainshtein, 1966),

$$< I(R) >= \mathrm{Re}[N(1+F)/(1-F)] - 2\,\mathrm{Re}[(F - F^{N+1})/(1-F)^2] \quad (19)$$

where

$$F = \exp(-2\pi^2 R^2 < \delta^2 >)\exp(i2\pi dR)$$

and *Re* refers to the real part of the function. When N is large, the second term is negligible, and (19) reduces to

$$< I(R) >= \frac{N(1-[H(R)]^2)}{1+[H(R)]^2 - 2[H(R)]\cos(2\pi dR)} \quad (20)$$

$$\text{with } H(R) = \exp(-2\pi^2 < \delta^2 > R^2).$$

Results & Discussion

X-ray diffraction from assemblies formed by prion-related peptides

The X-ray diffraction patterns of SHa106-122, SHa109-122 ("H1") (Nguyen *et al*., 1995; Inouye *et al*., 2000), and SHa113-120 (A8A) have been reported (Figure 3 and Table 1). SHa106-122 (Fig. 3A) and SHa109-122 (Fig. 3B) dried from 50% acetonitrile (AcN) solution show slightly oriented diffraction patterns while the lyophilized H1 (Fig. 3C) and A8A (Fig. 3D) dried from 50% AcN show powder patterns. The wide-angle reflections were indexed by a two-dimensional orthogonal lattice with a=9.5-9.6 Å and c=10.2-15.9 Å, where a is the hydrogen-bonding direction in the β sheet, and c is the intersheet direction. In the oriented patterns, the *(h0l)* reflections were accentuated on the meridian, indicating that the rotation axis is in the *b*-direction (or on the equator). Therefore, macroscopically the sample is slab-like, with the slabs stacked in the direction of the *b*-axis.

A strong low-angle reflection is observed at 73 Å for SHa106-122 (Fig. 3A; and Fig. 2A in Inouye *et al*., 2000), and at 40 Å for AcN-treated H1 (Fig. 3B; Table 1). In the former, subsequent broad intensity maxima are observed at 23 Å and 13 Å Bragg spacings. The strong reflection likely arises from a one-dimensional interference function *Z(R)* for the stacking of the slab-like structures with period *d*, and the broad maxima is from the Fourier transform of the unit slab of thickness *a* (Inouye *et al*., 2000). Considering the interference function of *Z(R)* as the average intensity function of the one-dimensional lattice with cumulative disorder (see above) - i.e., $<I(R)>$ in equation (20) - and using $<\delta^2> = \Delta^2$, the intensity function can be written as $I(R) = |F(R)|^2 Z(R)$, where R is the reciprocal coordinate of the real coordinate r along the slab stacking direction and the Fourier transform of a slab with thickness a is given by $F(R)=a\,\mathrm{sinc}(\pi aR)$. The parameters a = 33.6 Å and Δ = 18.5 Å for SHa106-122 having d = 73 Å were determined by searching for the minimum residual between the observed and calculated intensities (Inouye *et al*., 2000). The thickness of 33 Å gives a crucial constraint to the length of the extended β chain.

In the wide-angle region of the diffraction patterns the (201) reflection is strong, whereas the (200) reflection at ~4.7 Å Bragg spacing for A8A and for lyophilized H1 is much weaker or nonexistent, or for SHa106-122 and solubilized/dried H1 nearly as strong as the (201) reflection. This intensity distribution and the large lattice constant c indicate that the unit cell contains four β chains, and that neighboring β sheets are quarter-staggered in the hydrogen bonding direction (Figure 4A-D, left panels) as in β silk (Marsh *et al*., 1955). The intersheet distance is ~8 Å for SHa106-122 and solubilized/dried H1, but ~5 Å for lyophilized H1 and A8A. With the β silk backbone as an initial phase model, the structure amplitudes from the model were calculated, and compared with the structure amplitudes extracted from the observed intensity (Table 1). The electron density maps from the observed structure amplitudes and phases from the silk model for SHa106-122 and solubilized/dried H1 (Figure 4A,B: centre panels) show electron density peaks other than the ones expected from the peptide backbone. For lyophilized H1 and A8A the β silk backbone fit well with the observed electron density map (Figure 4C,D: centre panels). At this stage the *R*-factors (i.e., $R_{obs\text{-}amp}$) were 0.61 and 0.64 for SHa106-122 and solubilized/dried H1, 0.45 for

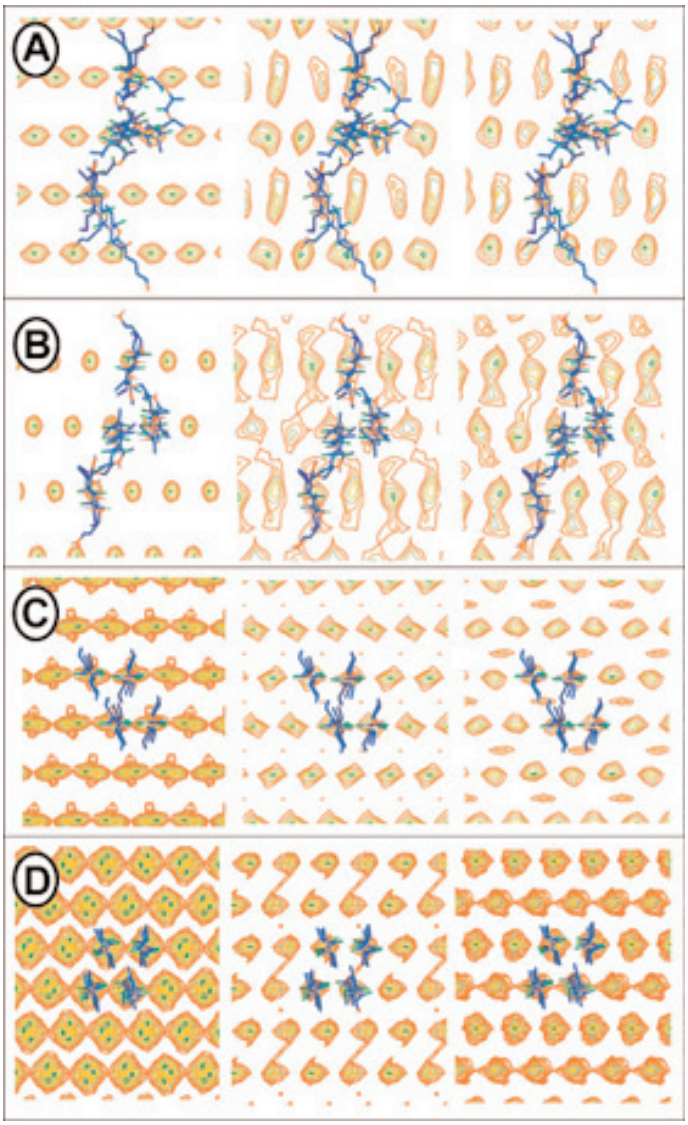

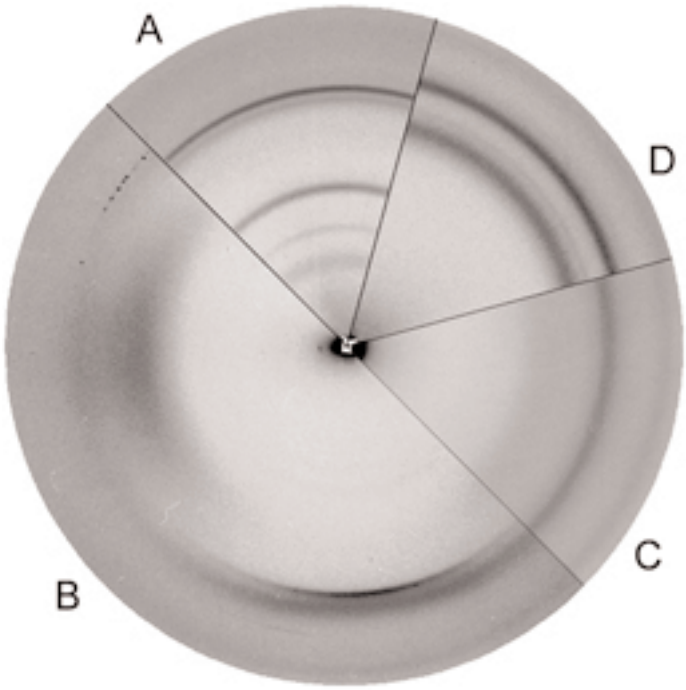

Figure 3. X-ray diffraction patterns of prion-related peptides. (A) SHa106-122 dried from 50% AcN. (A slight accentuation of the reflections was observed in the original diffraction pattern.); (B) H1 (SHa109-122) dried from 50% AcN; (C) lyophilized H1; and (D) A8A (SHa113-120) dried from 50% AcN. of SHa106-122 (Figure 2A in Inouye *et al*., 2000). Diffraction pattern (A) was previously reported by Inouye *et al*. (2000), and patterns (B)-(D) were reported by Nguyen *et al*. (1995). Note that the strongest reflection are: 4.56 Å (201) in (A); 4.77 Å (200) in (B); 4.44 Å (201) in (C); and 4.33 Å (201) in (D).

Figure 4. Electron density maps projected along the chain direction (*b*-axis) onto the plane defined by the H-bonding (*a*-axis; horizontal) and intersheet (*c*-axis; vertical) directions. (A) SHa106-122 dried from 50% AcN; (B) H1 domain dried from 50% AcN; (C) lyophilized H1; and (D) A8A. The unit cell projections in (A) and (B) contain two molecules, while the ones in (C) and (D) contain four molecules. The maps were calculated from: (*left*) amplitudes and phases from the initial model of β silk; (*center*) observed amplitudes and phases from β silk; and (*right*) observed amplitudes and phases from the prion model (shown as skeletal models for all maps). The contours show five levels of electron density; and the contour level steps were defined as one-tenth of the difference between the maximum and minimum electron densities, i.e., $\Delta\rho = (\rho_{max} - \rho_{main})/10$. The first contour level was given by $\rho_1 = \rho_{max} - \Delta\rho/2$, and subsequent ones were $\rho_2 = \rho_1 - \Delta\rho$, $\rho_3 = \rho_2 - \Delta\rho$, $\rho_4 = \rho_3 - \Delta\rho$, $\rho_5 = \rho_4 - \Delta\rho$. The *R*-factors for the initial silk model and the best prion model are indicated in Table 1.

lyophilized H1, and 0.33 for A8A (Table 1). The large R-factors for the first two peptides are probably due to not including in the initial model the side chains of the N-terminal domain. The molecular models of prion peptides including side chains were built and fit the electron density maps (Figure 4A-D, right panels).

Atomic models

In H1 (Figure 4B and 5A-C) the intra-chain turn creates two anti-parallel β-sheets, one that is constituted by the N-terminal larger residues, and the other by the alanine-rich region.. This structure agrees with the slab thickness as shown above and the larger and smaller electron density peaks. While three schematic molecular packings of H1 and SHa106-122 dried from AcN were suggested (Inouye *et al*., 2000), the structure amplitudes from the atomic models were not calculated in the past. We have now built the three models and rotated and translated the structures by XtalView to test them against the observed electron density maps (Figure 5A-C): in *Model 1*, the H1 molecules are registered, and the β chains are arranged anti-parallel (Figure 5A); in *Model 2* the H1 molecules are registered, and

Table 1. Summary of Bragg spacings (in Å) and *R*-factors from PrP-related peptides.

	Peptide			
	SHa106-122	H1 SHa109-122	H1 SHa109-122	A8A SHa113-120
Sample Preparation →	Dried from 50% AcN	Dried from 50% AcN	Lyophilized	Dried from 50% AcN
a (Å)	9.50	9.51	9.58	9.52
b (Å)	-	7.06	-	6.33
c (Å)	14.34	15.94	11.84	10.25
β (°)	90	88.41	90	90
$R_{obs\text{-}amp}$ (β-silk model)	0.61	0.64	0.45	0.33
$R_{obs\text{-}amp}$ (final)	0.34	0.24	0.36	0.36
	72.6 (Es)[a]	39.8 (Es)[a]	5.91 (Cw) (002)	31.9 (Cw)[a]
	23.2 (Ew)[b]	5.67 (Em) (110)	4.44 (Cs) (201)	5.13 (Cm) (002)
	12.8 (Ew)[b]	7.99 (Mw) (002)	3.73 (Cm) (202)	4.75 (Cw) (200)
	9,49 (Mw) (100)	4.77 (Ms) (200)	2.98 (Cvw) (004)	4.33 (Cs) (201)
	7.17 (Mm) (002)	4.57 (Mm) (201)		3.68 (Cw) (112)
	4.73 (Mm) (200)	3.94 (Mw) (004)		3.26 (Cvw)[c]
	4.56 (Ms) (201)	3.74 (Mm) (104)		2.82 (Cs)[c]
	3.19 (Cw) (300)	2.97 (Mw) (302)		
	2.86 (Cvw) (204)			

The Bragg spacings are cited in Inouye *et al*. (2000) for SHa106-122 dried from 50% AcN solution, and in Nguyen *et al*. (1995) for H1 (SHa109-122) lyophilized and dried from 50% AcN, and for A8A dried from 50% AcN. The unit cell lattice constants *a*, *b*, *c* and β are indicated, where *a*, *b* and *c* are in the H-bonding, β chain, and intersheet directions. The unit cell contains two β-chains in the H-bonding direction (along the *a*-axis) and two β-sheets in the intersheet direction (along the *c*-axis). (In Fig. 4, these correspond to the horizontal and vertical directions, respectively.) All the observed reflections in the oriented patterns of SHa106-122 and SHa109-122 (dried from 50% AcN) were indexed with the cylindrical (rotation) axis in the *b* direction. Because the meridional axis is defined to be in the direction of the ~4.7 Å H-bonding reflection, then the cylindrical axis in the oriented patterns is on the equator. The meridional location of the sharp (*h0l*) reflections indicates, therefore, that the scattering object is slab-like.

[a]These low-angle reflections likely arise from the interference between slab-like or fibrillar structures that are stacked.

[b]These broad intensity maxima likely arise from the Fourier transform of the slab-like unit.

[c]These reflections are likely from NaCl.

the N-terminal and C-terminal β chains are in a parallel β-sheet conformation (Figure 5B); and in *Model 3* the H1 molecules are staggered in the intersheet direction and the β chains are anti-parallel (Figure 4B, right, and 5C). The models were then used to calculate the structure factors for comparison with the observed amplitudes. The calculated *R*-factors ($R_{amp\text{-}obs}$) were found to be 0.46 for the anti-parallel registered arrangement, 0.37 for the parallel registered arrangement, and 0.24 for the staggered arrangement (Table 1). A similar staggered assembly of reverse-turn SHa106-122 molecules gave an R-factor of 0.34 (Figure 4A, right); and the atomic model for the N-terminal alanine-rich domain in lyophilized H1 (Figure 4C, right, and 5D) and for A8A gave similar R-factors of 0.36 (Figure 4D, right), which is nearly the same as the initial *R*-factor derived using the β silk backbone (Table 1).

Molecular interpretation

Lysine residues are spatially localized close to one another (as are histidine residues) in both the anti-parallel and parallel β chain models (Figure 5A,B); however, because of electrostatic repulsion, such arrangements may not be stable. In the staggered arrangement (Figure 5C), by contrast, the histidine and lysine residues are close together. If the positive-charged lysine residue is directed toward the aromatic ring of the histidine, the staggered arrangement may, in fact, be stabilized. In this arrangement His111 of one molecule is closely positioned to Lys110 of the neighboring molecule. The atomic model indicates that the neighboring residues of His111 are Ala113, Ala117, and Lys110. When a larger valine residue substitutes for Ala117 in the GSS mutation, His111 will interact with valine more strongly due to van der Waals contacts. Thus, in PrP having the GSS substitution the folded β sheet structure may be stabilized. The interaction between

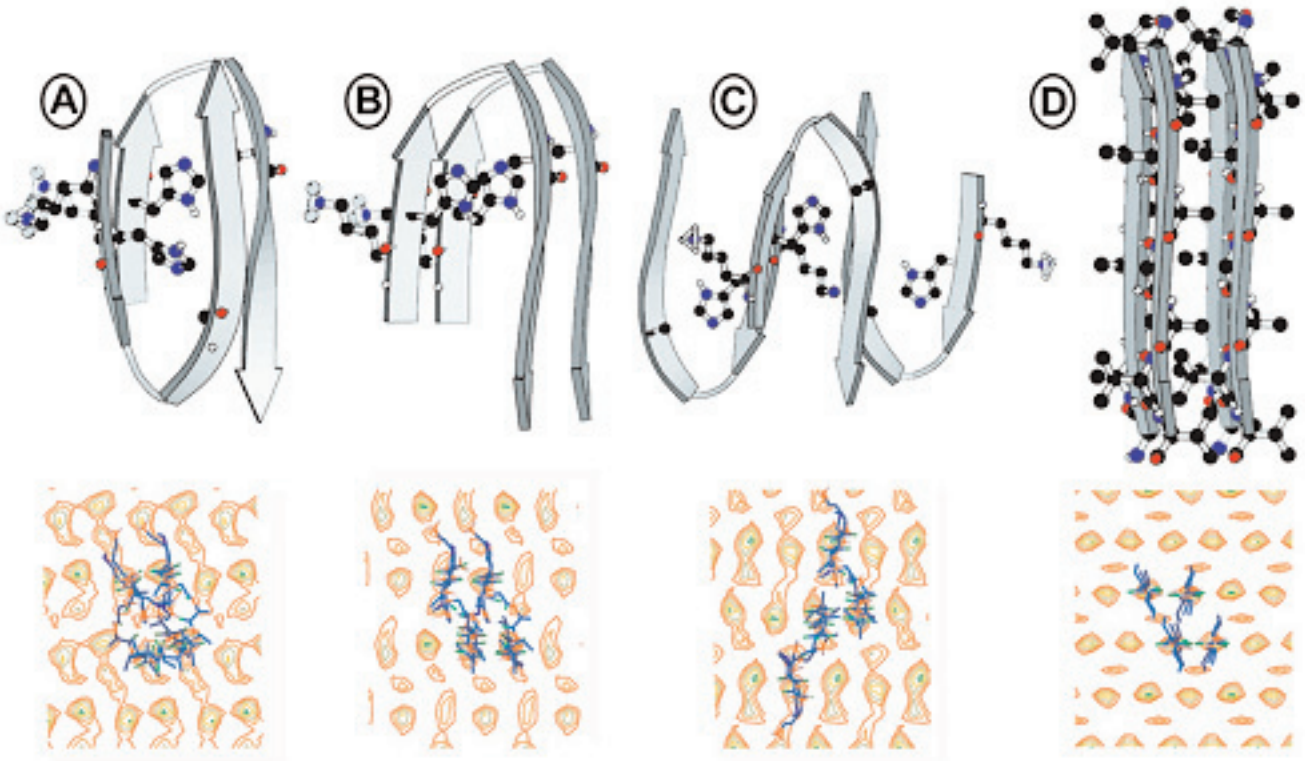

Figure 5. Molscript representations (*upper*) and electron density projections (*lower*) based on structural analysis of X-ray fibre diffraction patterns of H1 (SHa109-122). (A) anti-parallel, (B) parallel, and (C) staggered arrangement of H1 dried from 50% AcN; and (D) lyophilized H1. *Upper*: The molecular model which fits the observed electron density map shows two β chains, where Gly114-Ala115 are at the γ inverse turn (as defined by STRIDE; Frishman and Argos, 1995). Lys110, His111 and Ala117 are indicated by the ball and stick models. Note that the Lys side chains (and those of His) are close together in the anti-parallel and parallel arrangements while Lys and His are adjacent to one another in the staggered arrangement (C). In the lyophilized sample (D), the alanine-rich domain as a β strand fits the electron density distribution, and the 3F4 domain is likely disordered (not shown). *Lower*: XtalView representations of skeletal models superposed on the electron density projection along the chain direction of H1. H-bonding is horizontal, and the intersheet direction is vertical.

histidine and lysine is not unprecedented. For example, the NMR structure of CD59 (which inhibits formation of the membrane attack complex) shows that lysine interacts with histidine, and forms a motif that marks this complement regulator as a potential glycation target (Fletcher *et al*., 1994; Acosta *et al*., 2000).

Comparison with previous models of binding interface

Arguments based on sequence differences and the species barrier to prion infectivity have led to the suggestion that the 3F4 antibody-specific epitope (residues 109-112) is at the binding interface for the PrP^{C}-PrP^{Sc} heterodimer (Schätzl *et al*., 1995; Warwicker, 1997). The binding interface was established by identifying peptides that can inhibit the cell-free replication of PrP^{Sc}. Such peptides likely interact at the heterodimer interface and block the binding of PrP^{C} to PrP^{Sc}. Horiuchi *et al*. (2001) found that peptides SHa119-136, SHa166-179 and SHa200-223 inhibit the binding, and Chabry *et al* (1998) identified SHa106-141 as having a similar effect. Since the 3F4 epitope in the PrP^{Sc} isoform is not reactive to the antibody (Peretz *et al*., 1997), the molecular conformation of this region most likely changes when heterodimerization occurs, such that the domain becomes exposed on the surface of the protein. Previous molecular modelling (Warwicker, 2000) suggested that the interface is Ala118-Ala133 and that the corresponding domains of the two molecules interact with each other. This domain was modeled as a reverse-turn anti-parallel β chain with the turn at Gly126-Gly127. The side chain interaction in the intersheet direction was via H-bonding between the S atom of Met129 and N-H in Gly124, and via van der Waals interactions between Val122 side chains. This model, however, agrees neither with our model which shows the turn in the H1 domain (residues 109-122; γ inverse turn as indicated by STRIDE; Nguyen *et al*., 1995; Inouye and Kirschner, 1998) nor with the crystallographic finding of an Ω turn that involves residues 104-113 near the 3F4 epitope (Kanyo *et al*., 1999). While neighboring β chains appear to be hydrogen-bonded

to one another in most proteins (as in the PrP dimer: Warwicker, 2000), there are examples (like in H1) where the two β chains are not H-bonded but interact across the intersheet space, e.g., the Ω turn for the Fab3F4 epitope in prion (Kanyo *et al*., 1999), and turn II (residues 7-20) of bovine myelin P0-glycoprotein (Shapiro *et al*., 1996). Molecular dynamics simulation (Levy *et al*., 2001) also shows a similar reverse-turn model with the two chains interacting across the intersheet space of PrP106-126. A recent model of Alzheimer's β-protein in the amyloid fibril based on solid state NMR shows a similar folding (Tycko, 2003).

Conclusion

From an analysis of X-ray fibre diffraction patterns of prion-related peptides, we observed structural polymorphism (two different conformations) for the H1 domain - one folded and the other unfolded. In the former the 3F4 epitope region is a β chain, while in the latter the epitope does not assume this conformation and is likely to be exposed on the protein surface. The folded structure is stabilized by an interaction between His111 and Ala117. Cell-free replication of PrP requires a partial denaturation of PrP^{Sc} which exposes the 3F4 epitope domain on the protein surface. The conformational transformation, termed template breathing (Caspi *et al*., 1998), therefore, involves the folding → unfolding of the H1 domain. The intermolecular packing characterized by our fibre diffraction analysis indicates that the alanine-rich domains are hydrogen-bonded together, which may be the major binding force driving the interaction of PrP^{C} and PrP^{Sc}.

Acknowledgements

For discussions and/or collaborations over the past eight years that have contributed to our application of fibre diffraction to understanding the organization of PrP, we gratefully acknowledge Mr. J.P. Bond and Drs. J.T. Nguyen, R.J. Fletterick, F.E. Cohen, M.A. Baldwin, H.L. Ball, and S.B. Prusiner. The research in our lab was supported by an Alzheimer's Association/T.L.L. Temple Discovery Award (D.A.K.), the Alzheimer's Disease Research Program of the American Health Assistance Foundation (D.A.K.), and institutional support from Boston College.

References

[1] Acosta, J., Hettinga, J., Fluckiger, R., Krumrei, N., Goldfine, A., Angarita, L., & Halperin, J. (2000) Molecular basis for a link between complement and the vascular complications of diabetes. *Proc. Natl. Acad. Sci. USA* **97**, 5450-5455.

[2] Barakat, R. (1987) X-ray scattering from helical structures possessing random variable twist. *Acta. Cryst*. **A43**, 45-49.

[3] Caspi, S., Halimi, M., Yanai, A., Sasson, S.B., Taraboulos, A. & Gabizon, R. (1998) The anti-prion activity of Congo red. *J. Biol. Chem*. **273**, 3484-3489.

[4] Cella, R.J., Lee, B. & Hughes, R.E. (1970) Lorentz and orientation factors in fibre X-ray diffraction analysis. *Acta Cryst.* **A26**, 118-124.

[5] Chabry, J., Caughey, B., & Chesebro, B. (1998) Specific inhibition of in vitro formation of protease-resistant prion protein by synthetic peptides. *J. Biol. Chem.* **273**, 13203-13207.

[6] Donne, D.G., Viles, J.H., Groth, D., Mehlhorn, I., James, T.L., Cohen, F.E., Prusiner, S.B., Wright, P.E. & Dyson, H.J. (1997) Structure of the recombinant full-length prion protein PrP(29-231): The N terminus is highly flexible. *Proc. Natl. Acad. Sci. USA* **94**, 13452-13457.

[7] Egelman, E.H. & DeRosier, D.J. (1982) The Fourier transform of actin and other helical systems with cumulative random angular disorder. *Acta Cryst.* **A38**, 796-799.

[8] Fletcher, C.M., Harrison, R.A., Lachmann, P.J., & Neuhaus, D. (1994) Structure of a soluble, glycosylated form of the human complement regulatory protein CD59. *Structure*. **2**, 185-199.

[9] Frishman, D. & Argos, P. (1995) Knowledge-based protein secondary structure assignment. *Proteins*. **23**, 566-579.

[10] Guex, N., Diemand, A., & Peitsch, M.C. (1999) Protein modelling for all. *Trends Biochem. Sci*. **24**, 364-367.

[11] Horiuchi, M., Baron, G.S., Xiong, L.W., & Caughey, B. (2001) Inhibition of interactions and interconversions of prion protein isoforms by peptide fragments from the C-terminal folded domain. *J. Biol. Chem*. **276**, 15489-15497.

[12] Hosemann, R. & Bagchi, S.N. (1962) *Direct Analysis of Diffraction by Matter*, North-Holland Publishing Co., Amsterdam.

[13] Inouye, H. (1994) X-ray scattering from a discrete helix with cumulative angular and translational disorders. *Acta Cryst*. **A50**, 644-646.

[14] Inouye, H., Bond, J.P., Baldwin, M.A., Ball, H.L., Prusiner, S.B., & Kirschner, D.A. (2000) Structural changes in a hydrophobic domain of the prion protein induced by hydration and by Ala → Val and Pro → Leu substitutions. *J. Mol. Biol.* **300**, 1283-1296.

[15] Inouye, H., Fraser, P.E., & Kirschner, D.A. (1993) Structure of β-crystallite assemblies formed by Alzheimer β-amyloid protein analogues: Analysis by X-ray diffraction. *Biophys. J*. **64**, 502-519.

[16] Inouye, H., Karthigasan, J., & Kirschner, D.A. (1989) Membrane structure in isolated and intact myelins. *Biophys. J*. **56**, 129-137.

[17] Inouye, H. & Kirschner, D.A. (1996) Refined fibril structures: The hydrophobic core in Alzheimer's β-amyloid and prion as revealed by X-ray diffraction. *In: The Nature and Origin of Amyloid Fibrils*, Ciba Foundation Symposium No. 199, p. 22-39, John Wiley & Sons, Chichester, UK and New York, NY.

[18] Inouye, H. & Kirschner, D.A. (1997) X-ray diffraction analysis of scrapie prion: Intermediate and folded structures in a peptide containing two putative α-helices. *J. Mol. Biol*. **268**, 375-389.
[19] Inouye, H. & Kirschner, D.A. (1998) Polypeptide chain folding in the hydrophobic core of hamster scrapie prion: Analysis by X-ray diffraction. *J. Struct. Biol*. **122**, 247-255.
[20] James, T.L., Liu, H., Ulyanov, N.B., Farr-Jones, S., Zhang, H., Donne, D.G., Kaneko, K., Groth, D., Mehlhorn, I., Prusiner, S.B., & Cohen, F.E. (1997) Solution structure of a 142-residue recombinant prion protein corresponding to the infectious fragment of the scrapie isoform. *Proc. Natl. Acad. Sci. USA* **94**, 10086-10091.
[21] Kabsch, W., & Sander, C. (1983) Dictionary of protein secondary structure: Pattern recognition of hydrogen-bonded and geometrical features. *Biopolymers* **22**, 2577-2637
[22] Kanyo, Z.F., Pan, K.M., Williamson, R.A., Burton, D.R., Prusiner, S.B., Fletterick, R.J. & Cohen, F.E. (1999) Antibody binding defines a structure for an epitope that participates in the $PrP^{C} \rightarrow PrP^{Sc}$ conformational change. *J. Mol. Biol*. **293**, 855-63.
[23] Kitamoto, T., Iizuka, R. & Tateishi, J. (1993) An amber mutation of prion protein in Gerstmann-Sträussler syndrome with mutant PrP plaques. Biochem. *Biophys. Res. Commun.* **192**, 525-531.
[24] Knaus, K.J., Morillas, M., Swietnicki, W., Malone, M., Surewicz, W.K. & Yee, V.C. (2001) Crystal structure of the human prion reveals a mechanism for oligomerization. *Nature Struct. Biol*. **8**, 770-774.
[25] Kocisko, D.A., Come, J.H., Priola, S.A., Chesebro, B., Raymond, G.J., Lansbury, P.T. & Caughey, B. (1994) Cell-free formation of protease-resistant prion protein. *Nature* **370**, 471-474.
[26] Kraulis, P.J. (1991) MOLSCRIPT: A program to produce both detailed and schematic plots of protein structures. *J. Appl. Crystallogr*. **24**, 946-950.
[27] Levy, Y., Hanan, E., Solomon, B. & Becker, O.M. (2001) Helix-coil transition of PrP106-126: Molecular dynamic study. *Proteins: Structure, Function and Genetics*. **45**, 382-396.
[28] Liu, H., Farr-Jones, S., Ulyanov, N.B., Llinas, M., Marqusee, S., Groth, D., Cohen, F.E., Prusiner, S.B. & James, T.L. (1999) Solution structure of Syrian hamster prion protein rPrP(90-231). *Biochemistry* **38**, 5362-5377.
[29] Lopez Garcia, F., Zahn, R., Riek, R. & Wüthrich, K. (2000) NMR structure of the bovine prion protein. *Proc. Natl. Acad. Sci. USA* **97**, 8334-8339.
[30] Marsh, R.E., Corey, R.B. & Pauling, L. (1955) The structure of Tussah silk fibroin. *Acta Cryst*. **8**, 710-715.
[31] McRee, D.E. (1992) A visual protein crystallographic software system for X11/XView. *J. Mol. Graph*. **10**, 44-46.
[32] Nguyen, J.T., Inouye, H., Baldwin, M.A., Fletterick, R.J., Cohen, F.E., Prusiner, S.B. & Kirschner, D.A. (1995) X-ray diffraction of scrapie prion rods and PrP peptides. *J. Mol. Biol*. **252**, 412-422.
[33] Pan, K-M., Baldwin, M., Nguyen, J., Gasset, M., Serban, A., Groth, D., Mehlhorn, I., Huang, Z., Fletterick, R.J., Cohen, F.E. & Prusiner, S.B. (1993) Conversion of α-helices into β-sheets features in the formation of the scrapie prion proteins. *Proc. Natl. Acad. Sci. USA*. **90**, 10962-10966.
[34] Peretz, D., Williamson, R.A., Matsunaga, Y., Serban, H., Pinilla, C., Bastidas, R.B., Rozenshteyn, R., James, T.L., Houghten, R.A., Cohen, F.E., Prusiner, S.B. & Burton, D.R. (1997) A conformational transition at the N-terminus of the prion protein features in formation of the scrapie isoform. *J. Mol. Biol*. **273**, 614-622.
[35] Prusiner, S.B. (1991) Molecular biology of prion diseases. *Science* **252**,1515-1522.
[36] Prusiner, S.B., McKinley, M.P., Bowman, K.A., Bolton, D.C., Bendheim, P.E., Groth, D.F. & Glenner, G.G. (1983) Scrapie prions aggregate to form amyloid-like birefringent rods. **Cell 35**, 349-358.
[37] Riek, R., Hornemann, S., Wider, G., Billeter, M., Glockshuber, R. & Wüthrich, K. (1996) NMR structure of the mouse prion protein domain PrP(121-231). *Nature* **382**, 180-182.
[38] Safar, J., Wille, H., Itri, V., Groth, D., Serban, H., Torchi, M., Cohen, F.E. & Prusiner, S.B. (1998) Eight prion strains have PrP^{Sc} molecules with different conformations. *Nature Med*. **4**, 1157-1165.
[39] Schätzl, H.M., DaCosta, M., Taylor, L., Cohen, F.E., & Prusiner, S.B. (1995) Prion protein gene variation among primates. *J. Mol. Biol*. **245**, 362-374.
[40] Shapiro, L., Doyle, J.P., Hensley, P., Colman, D.R. & Hendrickson, W.A. (1996) Crystal structure of the extracellular domain from P0, the major structural protein of peripheral nerve myelin. *Neuron* **17**, 435-449.
[41] Stahl, N., Baldwin, M.A., Teplow, D.B., Hood, L., Gibson, B.W., Burlingame, A.L. & Prusiner, S.B. (1993) Structural analysis of the scrapie prion protein using mass spectroscopy and amino acid sequencing. *Biochemistry* **32**, 1991-2002.
[42] Tycko, R. (2003) Insights into the amyloid folding problem from solid-state NMR. *Biochemistry* **42**, 3151-3159.
[43] Vainshtein, B.K. (1966) *Diffraction of X-rays by Chain Molecules*. Amsterdam: Elsevier.
[44] Viles, J.H., Cohen, F.E., Prusiner, S.B., Goodin, D.B., Wright, P.E. & Dyson, H.J. (1999) Copper binding to the prion protein: Structural implications of four identical cooperative binding sites. *Proc. Natl. Acad. Sci. USA* **96**, 2042-2047
[45] Warwicker, J. (1997) Species barriers in a model for specific prion protein dimerization. Biochem. *Biophys. Res. Commun*. **232**, 508-512.
[46] Warwicker, J. (2000) Modelling a prion protein dimer: Predictions for fibril formation. Biochem. *Biophys. Res. Commun*. **278**, 646-652.
[47] Zahn, R., Liu, A.Z., Luhrs, T., Riek, R., von Schroetter, C., Garcia, F.L., Billeter, M., Calzolai, L., Wider, G. & Wüthrich, K. (2000) NMR solution structure of the human prion protein. *Proc. Natl. Acad. Sci. U.S.A.* **97**, 145-150.